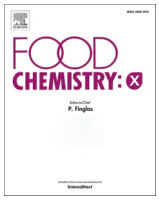
Food Chemistry: X 37 (2026) 104116



Contents lists available at ScienceDirect

Food Chemistry: X

journal homepage: www.sciencedirect.com/journal/food-chemistry-x



One-step microwave-assisted synthesis of nitrogen-doped carbon quantum dots for highly sensitive and selective fluorescence detection of mercury (II) ion in food

Jinlong Liu [a], Haotian Jiang [a], Chen Zhao [b], Hongda Li [a,c,*], Zongbin Li [d], Rui Zhang [e,**]

[a] College of Criminal Science and Technology, Criminal Investigation Police University of China, Shenyang 110035, China
[b] Department of Chemical Engineering, KU Leuven, Celestijnenlaan 200F, B-3001 Leuven, Belgium
[c] Criminal Investigation Detachment, Shenyang Public Security Bureau, Shenyang 110000, China
[d] Fuzhou Public Security Bureau, Fuzhou 350500, China
[e] Shenyang Key Laboratory of Medical Molecular Theranostic Probes in School of Pharmacy, School of Pharmacy, Shenyang Medical College, Shenyang 110034, China

ARTICLE INFO

Keywords:
Nitrogen-doped carbon quantum dots
N-CQDs
Fluorescent materials
Microwave-assisted synthesis
Hg^{2+} detection

ABSTRACT

To realize the low-cost preparation of Nitrogen-doped carbon quantum dots (N-CQDs) for high-sensitivity Hg^{2+} fluorescence detection and their application in food sample analysis, this study used malonic acid as the carbon source and 2,3-diaminopyridine as the nitrogen source to prepare N-CQDs via a one-step microwave-assisted heating method by optimizing the synthesis conditions. The surface functional groups, molecular structure, optical properties, and Hg^{2+} response characteristics of the N-CQDs were investigated in detail. Finally, the N-CQDs were applied for Hg^{2+} detection in typical real samples (tap water, rice, and grass shrimp). This study provides new insights and methods for clarifying the structure-activity relationship between N-CQDs and Hg^{2+} response, and constructing a rapid and accurate Hg^{2+} fluorescence probe detection system.

1. Introduction

Mercury is a typical heavy metal that exists in three valence states in nature: 0, +1, and +2. Among them, Mercury (II) ion (Hg^{2+}) is the most common form of mercury in oxidizing environments, and the accumulation mechanism of Hg^{2+} in the food chain deserves special attention (Ge et al., 2024). Aquatic organisms (e.g., fish and shellfish) absorb Hg^{2+} from water through their gills and body surfaces, and bio-transform it into the highly toxic methylmercury, and then enriched in organisms at higher trophic levels of the food chain via biomagnification (Yang, Qi, et al., 2023). Crops such as rice primarily take up mercury ions from contaminated soil and irrigation water. Studies have shown that the bioaccumulation factor of mercury in rice can reach 0.5 or higher biomagnification (Yang, Qi, et al., 2023). The bioaccumulation effect means that even low environmental mercury concentrations may cause excessive mercury levels in food, posing a threat to consumer health. Therefore, developing rapid detection methods suitable for complex food matrices is of great practical significance.

Current international food safety standards impose strict limits on Hg content. For instance, the European Union specifies that the total mercury limit in fish ranges from 0.5 to 1.0 mg/kg (EU 2023/915) (European Commission, 2023), while China's national standard GB 2762–2022 sets the total mercury limit in rice at 0.02 mg/kg (Lao et al., 2023). Traditional Hg detection techniques, including atomic absorption spectrometry, atomic emission spectrometry, inductively coupled plasma mass spectrometry, and electrochemical methods (Liu et al., 2024). However, these methods generally rely on specialized instrumentation and trained operators, leading to obvious limitations in on-site rapid detection scenarios and the practical demand for rapid and accurate responses. In parallel, emerging non-thermal processing technologies such as induced electric fields have shown promise in microbial inactivation in liquid foods, underscoring the ongoing innovation in food safety interventions (Zhang et al., 2025). Therefore, establishing an Hg^{2+} detection method with rapidity, low cost, and simplicity is of great practical importance.

Carbon quantum dots (CQDs), as a new type of zero-dimensional

* Corresponding author at: College of Criminal Science and Technology, Criminal Investigation Police University of China, Shenyang 110035, China.
** Corresponding author at: Shenyang Key Laboratory of Medical Molecular Theranostic Probes in School of Pharmacy, School of Pharmacy, Shenyang Medical College, Shenyang 110034, PR China.
E-mail addresses: lhd870821@163.com (H. Li), ruizhang@symc.edu.cn (R. Zhang).

https://doi.org/10.1016/j.fochx.2026.104116
Received 8 November 2025; Received in revised form 28 March 2026; Accepted 17 June 2026
Available online 18 June 2026
2590-1575/© 2026 The Authors. Published by Elsevier Ltd. This is an open access article under the CC BY-NC-ND license (http://creativecommons.org/licenses/by-nc-nd/4.0/).

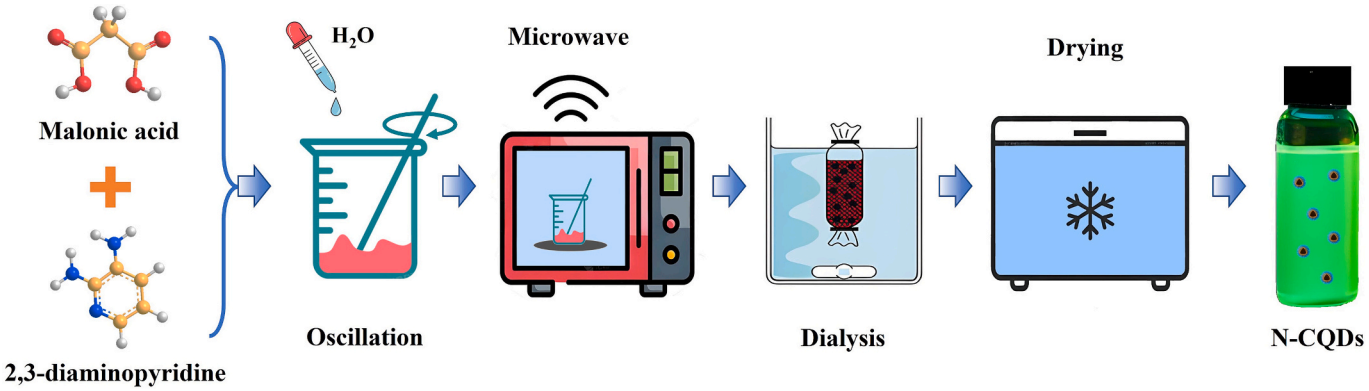


Fig. 1. Schematic diagram of the N-CQDs preparation process.

nanomaterial with a particle size ranging from 1 to 10 nm, possess excellent photoluminescent properties and surface effects due to their unique nanoscale size, along with good biocompatibility and extremely low cytotoxicity (Rani & Shanker, 2025). These advantages enable their safe application in on-site rapid fluorescence detection while avoiding the environmental safety issues of traditional organic and rare-earth fluorescent materials. Since their first synthesis in 2004 (Das et al., 2025), CQDs have shown great application potential in the field of rapid quantitative detection of pollutants. Heteroatom doping is an effective approach to enhance the fluorescent properties of CQDs. Heteroatom doping can modify the electronic energy level structure of CQDs, reduce surface defects, thereby improving the fluorescence quantum yield and enhancing luminescence performance (Bernalte et al., 2020). Meanwhile, it introduces new functional groups to improve the selectivity of CQDs. Among various heteroatoms, nitrogen is considered the optimal choice for CQDs doping due to its similar valence electron structure and atomic size to carbon (Xu et al., 2004).

Existing studies have reported the application of nitrogen-doped carbon quantum dots (N-CQDs) for Hg^{2+} detection. Pajewska-Szmyt et al. synthesized N-CQDs via a solid-state thermal method, which was successfully applied for Hg^{2+} detection in breast milk with good selectivity and high linearity (Pajewska-Szmyt et al., 2020), its limit of detection (LOD) was relatively high (0.44 μmol/L). Yang et al. prepared diethylenetriamine-β-cyclodextrin-modified N-CQDs for Hg^{2+} detection, showing good selectivity and low cytotoxicity (Yang, Yang, & Su, 2023), but the method was not applied to real sample detection. Barvin et al. developed a differential pulse voltammetry method using CQD-modified glassy carbon electrodes for Hg^{2+} detection, achieving a low LOD of 2.5 nmol/L and a good linear range of 0.5–300 nmol/L. (Barvin et al., 2019) However, due to limitations in material preparation processes and synthesis costs, large-scale promotion in environmental and food safety detection fields is difficult.

To realize the low-cost preparation of N-CQDs for high-sensitivity Hg^{2+} fluorescence detection and their application in real sample analysis, this study used malonic acid as the carbon source and 2,3-diaminopyridine as the nitrogen source to prepare N-CQDs via a one-step microwave-assisted heating method by optimizing the synthesis conditions. The surface functional groups, molecular structure, optical properties, and Hg^{2+} response characteristics of the N-CQDs were investigated in detail. Finally, the N-CQDs were applied for Hg^{2+} detection in typical real samples (tap water, rice, and grass shrimp). This study provides new insights and methods for clarifying the structure-activity relationship between N-CQDs and Hg^{2+} response, and constructing a rapid and accurate Hg^{2+} fluorescence probe detection system.

2. Experimental section

2.1. Chemicals and reagents

2,3-Diaminopyridine (purity ≥99%) and malonic acid (purity ≥98%) purchased from Shanghai Macklin Biochemical Co., Ltd. were used for N-CQDs preparation. Metal salts including $HgCl_2$, $CaCl_2$, $CuSO_4{\cdot}5H_2O$, $MnSO_4{\cdot}4H_2O$, $BaCl_2{\cdot}2H_2O$, $PbCl_2$, $CdCl_2$, $CrCl_2{\cdot}6H_2O$, $AlCl_3$, KCl, $CoCl_2{\cdot}6H_2O$, and $MgCl_2{\cdot}6H_2O$ were purchased from Sinopharm Chemical Reagent Co., Ltd. (China). A 50 μmol/L metal ion solution was prepared using deionized water (conductivity: 0.055 μS/cm) for testing the selectivity of N-CQDs toward Hg^{2+}. Concentrated HCl and NaOH (Sinopharm Chemical Reagent Co., Ltd.) were used to adjust the solution pH. All reagents used in this experiment are of analytical grade.

2.2. Instruments and equipment

N-CQDs were synthesized using a microwave reactor (Galanz G80D23CSP-Q5, China) with a fixed output power of 600 W and a fixed frequency of 2.45GHz. The reaction proceeded under atmospheric pressure, and the temperature was a resultant effect of the microwave irradiation time and power. The morphology and microstructure of the prepared N-CQDs were characterized by transmission electron microscopy (TEM, JEOL F200, Japan) operating at an acceleration voltage of 200 kV. For TEM analysis, a drop of diluted N-CQDs aqueous dispersion was deposited onto a copper grid and dried at room temperature. The elemental composition of N-CQDs was analyzed by X-ray photoelectron spectroscopy (XPS, Thermo Scientific ESCALAB 250Xi, USA). The chemical structure was further investigated using Fourier transform infrared spectroscopy (FT-IR, Thermo Fisher Scientific, USA). UV–Vis absorption spectra were recorded on a UV–Vis spectrophotometer (SHIMADZU UV-2550, Japan) using a 1 cm quartz cuvette, with a scanning range of 200–800 nm. Photoluminescence (PL) measurements were performed on a Cary Eclipse fluorescence spectrophotometer (G9800A, Agilent Technologies, USA) equipped with a 10 mm quartz cell. A pH meter (Sartorius PB-10, Germany) was used to prepare and measure solutions with different pH values.

2.3. Preparation of N-CQDs

The preparation process of N-CQDs is shown in Fig. 1. Briefly, 0.4 g of 2,3-diaminopyridine, 0.4 g of malonic acid, and 10 mL of deionized water were added to a beaker and stirred uniformly with a glass rod. The beaker was then placed in a microwave reactor for reaction. After the reaction, the beaker was cooled to room temperature, and 20 mL of deionized water was added. The mixture was ultrasonicated for 15 min, and the resulting solution was filtered through a 0.22 μm membrane to remove large particles. The filtrate was dialyzed in deionized water using a 3500 Da dialysis bag for 24 h. Finally, the dialyzed solution was

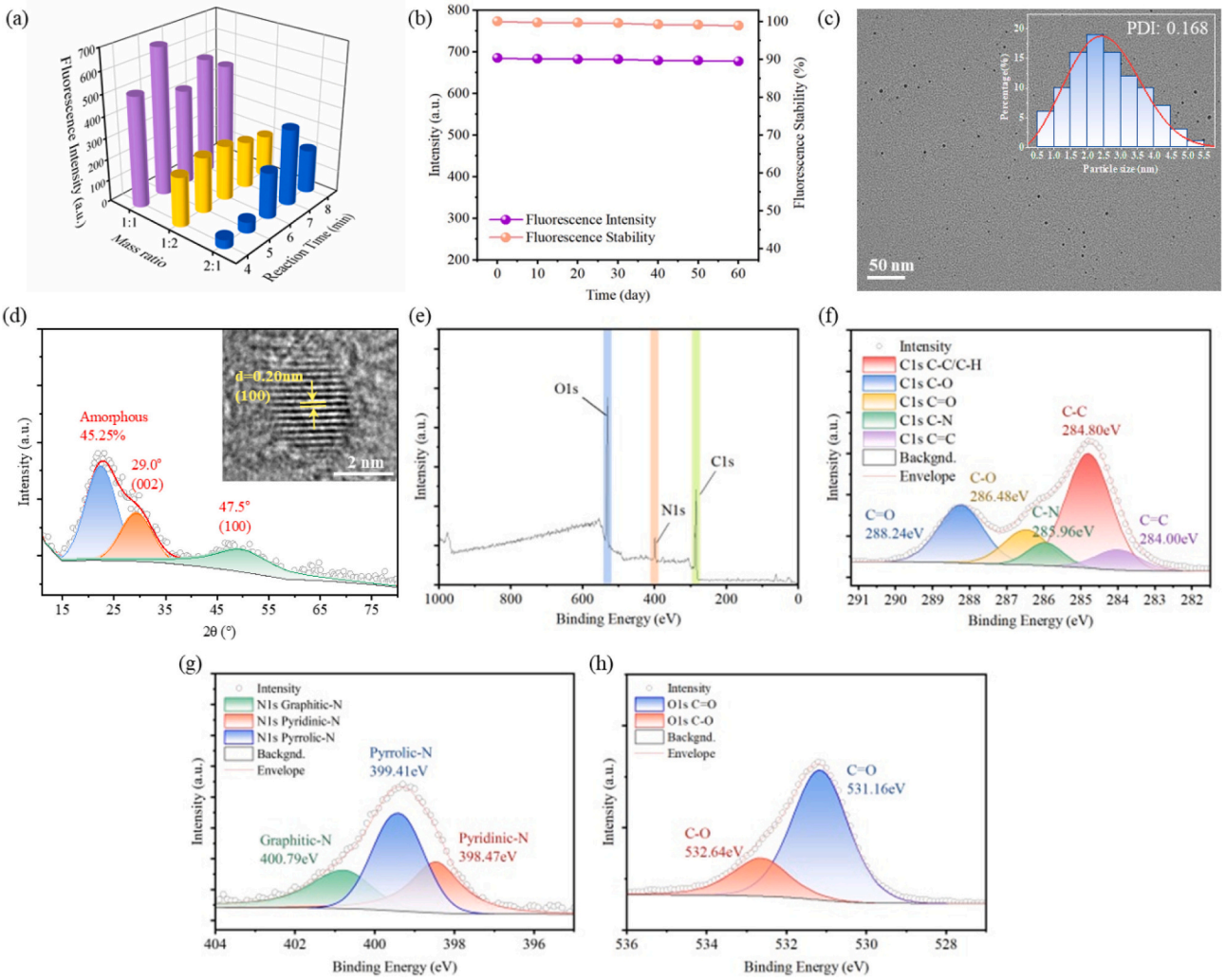


Fig. 2. (a) Effects of synthesis time and mass ratio of 2,3-diaminopyridine to malonic acid on the fluorescence intensity of N-CQDs; (b) Fluorescence stability of N-CQDs; (c) Transmission electron microscopy (TEM) image of N-CQDs; (d) XRD pattern of N-CQDs; (e)XPS Survey spectra of N-CQDs; (f) C1s; (g) N1s; (h) O1s.

freeze-dried to obtain N-CQDs powder.

2.4. Detection of Hg^{2+} using N-CQDs

2.4.1. Preparation of Hg^{2+} standard curve

$HgCl_2$ solutions with a series of concentrations (1, 2, 3, 4, 5, 6, 7, 8, 9, 10, 25, 50 μmol/L) were prepared. Under an excitation wavelength of 423 nm, the fluorescence intensity of the blank N-CQDs solution (F_0) and the fluorescence intensity of N-CQDs in $HgCl_2$ solutions with different concentrations (F) were measured. The Hg^{2+} standard curve was plotted with Hg^{2+} concentration (c(Hg^{2+}), μmol/L) as the abscissa and 1-F/F_0 as the ordinate.

2.4.2. Determination of Hg^{2+} via N-CQDs

To verify the selectivity of Hg^{2+} toward N-CQDs fluorescence quenching, 2.5 mg of N-CQDs powder was diluted to 100 mL to prepare a 25 mg/L N-CQDs stock solution, which was stored at 4 °C. For selectivity testing, N-CQDs solution (25 μmol/L), Hg^{2+} and interfering ion solutions (10 μmol/L) were mixed with phosphate-buffered saline (PBS, pH 7.0).

The pretreatment of actual food samples was performed by the following method. 2 g of *Fenneropenaeus chinensis*, rice and tap water samples were separately homogenized. Then 0.1 g of food homogenate were diluted by 5 mL of deionized water. After vortex mixing, the mixture was extracted in a 90 °C water bath for 30 min. After cooling, it was centrifuged at 10,000 rpm for 10 min, and the supernatant was filtered through a 0.22 μm microporous membrane. The N-CQDs solution was mixed with different sample solutions and PBS buffer, and fluorescence detection was performed under an excitation wavelength of 423 nm.

2.4.3. Modeling and computational details

The representative model of N-doped carbon quantum dots was constructed based on reported structural features of carbon-based nanomaterials with N-doping (Liu et al., 2025). The model consisted of a planar carbon skeleton (ca. 40–50 atoms) with a mixed sp^2/sp^3 hybridization, simulating the partially aromatic and partially saturated characteristics of N-CQDs. Pyridinic N, Graphitic N, and amino groups ($-NH_2$) were introduced into the carbon framework to simulate N-doping configurations. Surface functional groups, including C═O and -CH_2 were added to reflect the chemical diversity of N-CQDs. All density functional theory (DFT) calculations were performed using the Quantum ESPRESSO package (Giannozzi et al., 2017) The detailed computational information is described in Supporting Information.

3. Results and discussion

3.1. Optimization of preparation and synthesis conditions

To investigate the effect of different microwave synthesis conditions

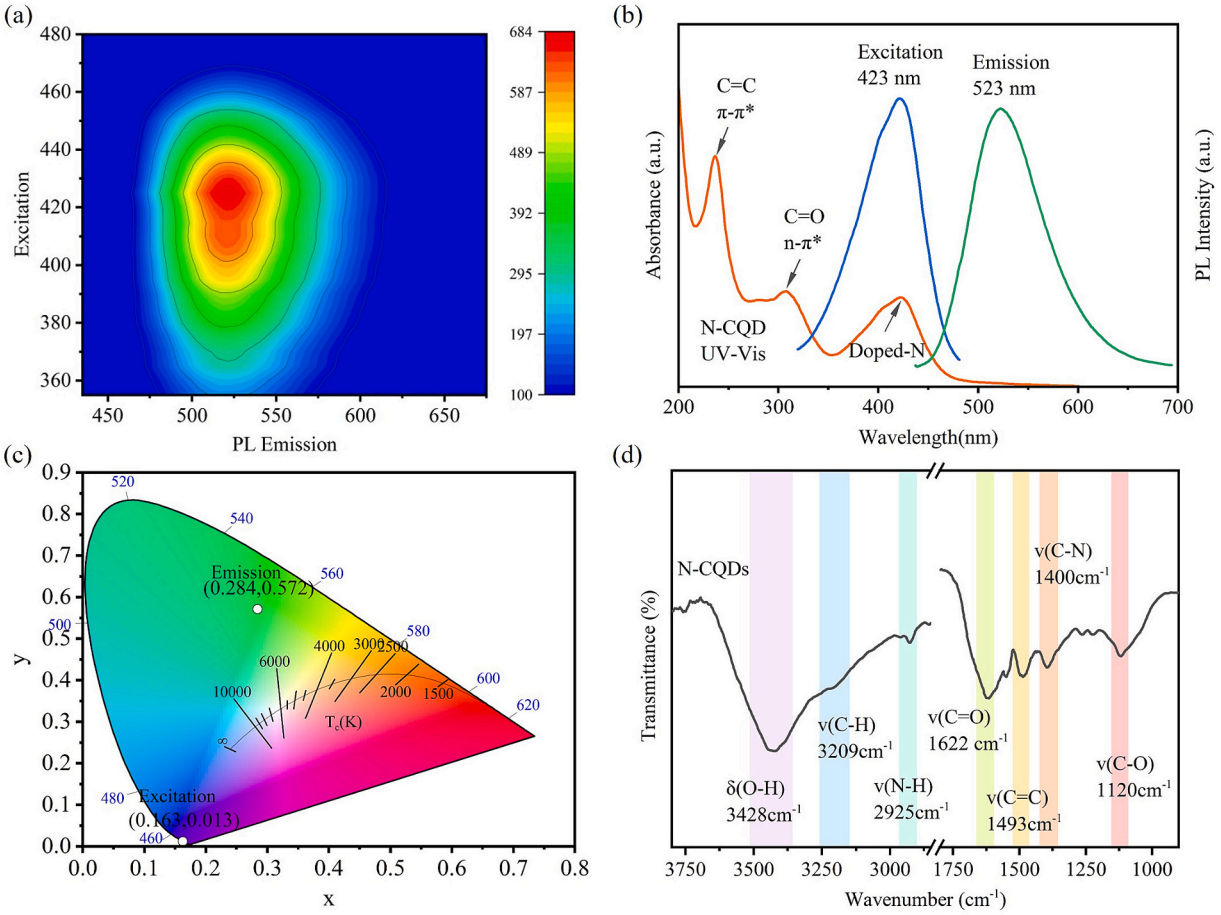


Fig. 3. (a) 3D fluorescence contour map of N-CQDs; (b) UV–Vis absorption spectrum of N-CQDs; (c) CIE 1931 chromaticity diagram of N-CQDs; (d) FT-IR spectrum of N-CQDs.

on the performance of N-CQDs, the fluorescence intensity of N-CQDs was measured under different reaction times and precursor ratios. As shown in Fig. 2(a), The synthesis conditions for N-CQDs were optimized to achieve maximum fluorescence intensity, which is directly correlated with the sensing performance. Specifically, reaction times ranging from 4 to 8 min were tested, while the mass ratio of 2,3-diaminopyridine to malonic acid was varied between 1:2, 1:1, and 2:1. As graphically represented in Fig. 2(a), the highest fluorescence intensity was consistently observed when a 1:1 mass ratio of 2,3-diaminopyridine to malonic acid was used and reacted for 5 min. With the extension of synthesis time, the fluorescence intensity gradually decreased. This phenomenon was attributed to the excessive growth and graphitization of the carbon core caused by prolonged reaction time, which led to cross-linking of N-CQDs to form larger aggregates (Hu, Tan, & Wang, 2024). Larger aggregates reduce the effective surface area and decreased the band gap of the carbon core. The absorbed ultraviolet light underwent non-radiative transitions, resulting in a decrease in the fluorescence quantum yield of N-CQDs.

The effect of precursor ratio showed that the synthesized N-CQDs exhibited the best fluorescence performance when the mass ratio of 2,3-diaminopyridine to malonic acid was 1:1. The fluorescence of N-CQDs is influenced by their surface functional groups such as -C-NH_2, -OH, and -C=O (Hu, Li, & Gong, 2024; Wu et al., 2023). These groups can themselves act as emission centers, and can also alter the electron cloud density at the carbon core interface. Therefore, adjusting the dosage of 2,3-diaminopyridine and malonic acid regulated the ratio of surface functional groups of N-CQDs, further optimizing the fluorescence intensity.

Under the optimized reaction time and precursor ratio, the fluorescence stability of the synthesized N-CQDs was further tested. As shown in Fig. 2(b), the fluorescence intensity of the N-CQDs solution only decreased by 1% after storage at 4 °C for 60 days, indicating good optical stability. Therefore, the N-CQDs were prepared using a 1:1 mass ratio of 2,3-diaminopyridine to malonic acid and a reaction time of 5 min for subsequent detection experiments.

3.2. *Structure and functional groups of N-CQDs*

The TEM image of the synthesized N-CQDs are shown in Fig. 2(c). The microwave-assisted synthesized N-CQDs exhibited a regular spherical morphology with uniform dispersion. The particle size distribution ranged from 0.5 to 5.5 nm, an average diameter of 2.81 nm. The N-CQDs exhibited a polydispersity index (PDI) of approximately 0.168, indicating a relatively narrow size distribution and good monodispersity. This small and uniform particle size is beneficial for obtaining fluorescence emission spectra with narrower full width at half maximum (FWHM) and more symmetric shape, thereby producing pure fluorescence color (Guo et al., 2024).

The XRD result of N-CQDs in Fig. 2(d) showed a interplanar spacing of 0.20 nm, corresponding to the characteristic lattice fringes of sp^2-hybridized graphitic carbon in the TEM image (Wang et al., 2024). This result indicated that the prepared N-CQDs had good crystallinity, which contributed to a more stable chemical structure, better resistance to photodamage, and maintenance of stable fluorescence signals under prolonged irradiation, thus achieving a higher fluorescence quantum yield.

X-ray photoelectron spectroscopy (XPS) was used to analyze the elemental composition and functional groups of N-CQDs. The survey of

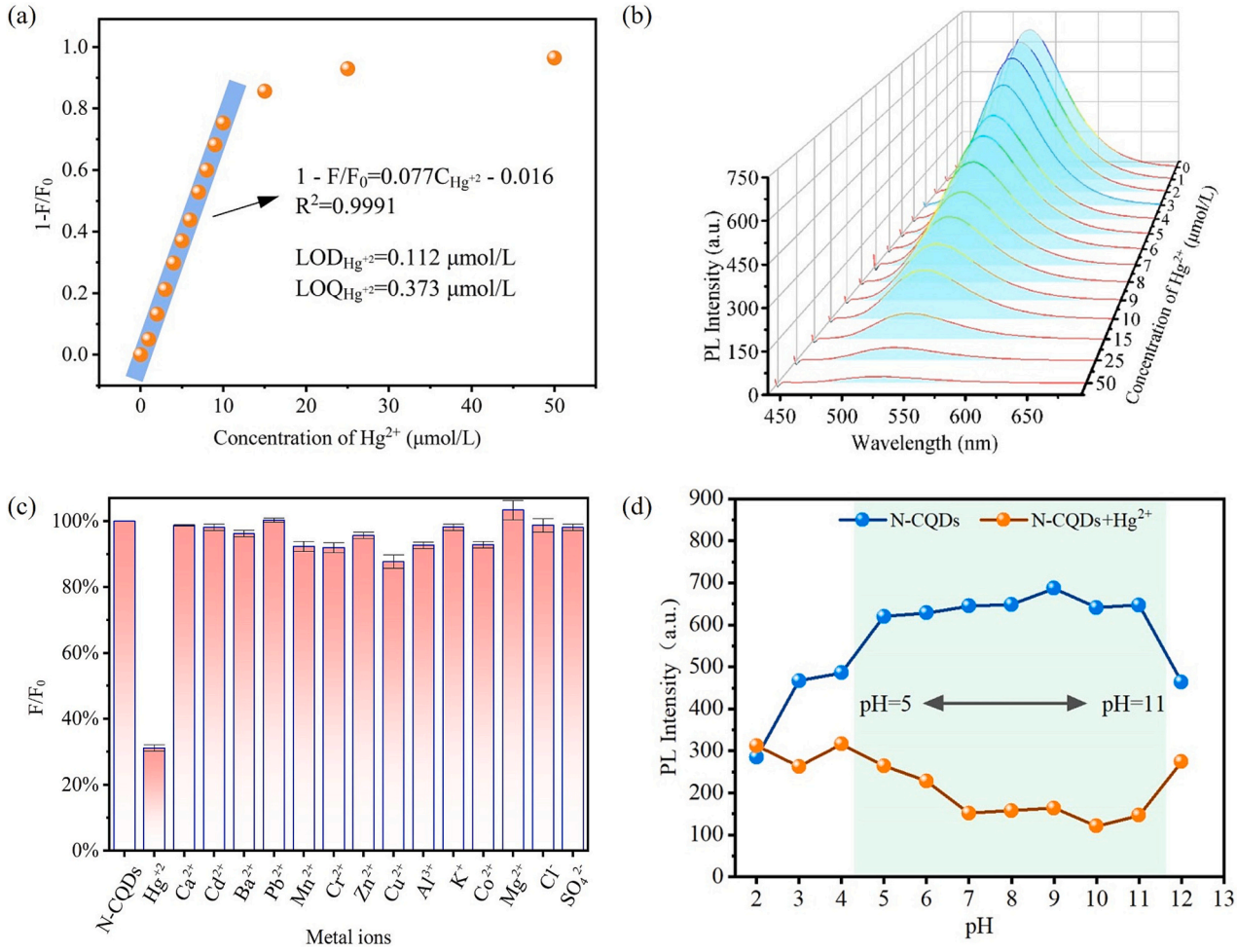


Fig. 4. (a) Linear relationship between Hg^{2+} concentration and fluorescence intensity in the range of 0–10 μmol/L; (b) Fluorescence spectra of N-CQDs under different Hg^{2+} concentrations; (c) Selectivity of Hg^{2+} toward N-CQDs fluorescence quenching; (d) Effect of different pH values on the fluorescence quenching efficiency of N-CQDs.

XPS spectrum in Fig. 2(e) showed that the N-CQDs only contained C, N, and O, with atomic percentages of 59.04%, 15.92%, and 25.03%, respectively. This confirmed that nitrogen atoms from 2,3-diaminopyridine were successfully doped into the N-CQDs.

The high-resolution XPS spectrum of C1s in Fig. 2(f) exhibited five characteristic peaks at 284.10 eV, 284.80 eV, 285.96 eV, 286.48 eV, and 288.24 eV, which were assigned to graphitic carbon (Baslak et al., 2023), C—C, C—N, C—O, and C═O groups (Yang, Wang, & Zhao, 2023), respectively. This result indicated that the carbon framework of N-CQDs contained not only sp^2-hybridized graphitic carbon but also abundant carbon-containing functional groups on the surface. The high-resolution spectrum of N1s in Fig. 2(g) showed three sub-peaks at 398.5 eV, 399.4 eV, and 400.9 eV, corresponding to pyridinic N, C-NH_2, and graphitic N (Xu et al., 2024), respectively. This suggested that nitrogen atoms were not only doped into the carbon core framework but also existed on the N-CQDs surface in the form of C-NH_2. The high-resolution spectrum of O1s in Fig. 2(h) revealed two chemical states of oxygen in N-CQDs: C═O (531.2 eV) and C—O (532.8 eV) (Ning et al., 2022). This was evidence of oxygen incorporation into the N-CQDs structure and the participation of malonic acid in the N-CQDs synthesis reaction. The XPS results confirmed that the prepared N-CQDs were rich in functional groups such as C═O, C—O, C—N, and C-NH_2 (Msto et al., 2023; Shabbir et al., 2023). The fluorescence of N-CQDs strongly depends on these surface functional groups, which can either act as emission centers and or optimize luminescence by modifying the electron cloud density of the carbon core (Arul et al., 2023; Yu et al., 2025), thereby improving the sensitivity of N-CQDs for Hg^{2+} fluorescence detection. This functional group-mediated sensing approach is consistent with advanced material-based detection strategies, used in colorimetric sensor arrays for selective analyte recognition (Hong et al., 2022).

3.3. *Spectroscopic properties of N-CQDs*

The optical properties of N-CQDs directly determine their application methods. Fig. 3(a) shows the 3D fluorescence contour map of N-CQDs in pure water. It can be observed that the excitation wavelengths of N-CQDs were concentrated in the range of 400–440 nm, and excitation wavelength-independent emission peaks were observed in the range of 500–540 nm.

Fig. 3(b) shows the UV–Vis absorption spectrum of N-CQDs, with three main absorption peaks. The absorption peaks at 239 nm and 307 nm were attributed to the π-π* transition of C═C (Msto et al., 2023) and the n-π* transition of C═O (Othman, Anwer, & Ali, 2024), respectively. A strong absorption peak at 423 nm was assigned to the conjugated structure of the nitrogen-doped carbon core (Wu et al., 2024), which was consistent with the XPS analysis results of the occurrence forms of C, N, and O. Importantly, the position of the UV–Vis absorption peak at 423 nm completely coincided with the maximum excitation peak observed at 423 nm in the fluorescence excitation spectrum. This clearly indicated that 423 nm was an effective excitation channel for N-CQDs to produce fluorescence, and the luminescence originated from the intrinsic state emission of the nitrogen-doped carbon core itself rather than surface

group or defect states. Nitrogen doping constructed a conjugated structure with clear optical activity.

The CIE 1931 chromaticity diagram of N-CQDs in Fig. 3(c) intuitively demonstrated its optical properties. First, the excitation point was located at coordinates (0.163, 0.013), corresponding to an excitation wavelength of 423 nm, indicating that N-CQDs could be effectively excited by visible light in this wavelength range. Second, the emission point was located at (0.284, 0.572) in the green region of the chromaticity diagram. The emission point was located in the green region and far from the center, suggesting high color purity of the green fluorescence of N-CQDs.

The FT-IR spectrum of N-CQDs in Fig. 3(d) showed a broad absorption peak at 3428 cm^{-1}, which was assigned to the bending vibration of -OH (Prayugo & Gea, 2023). The absorption peaks at 3209 cm^{-1} and 2925 cm^{-1} were attributed to the stretching vibrations of ν(C—H) (Saravanan et al., 2024) and ν(N—H) (Wu et al., 2025), respectively. The absorption peaks at 1622 cm^{-1} and 1493 cm^{-1} corresponded to the stretching vibrations of ν(C=O) (Keerthana et al., 2023) and ν(C=C) (Kundu et al., 2025), respectively. In addition, the absorption peak at 1400 cm^{-1} was assigned to the stretching vibration of ν(C—N) (Zhang et al., 2024), and the characteristic absorption peak at 1120 cm^{-1} was caused by the stretching vibration of ν(C—O) (Rawat et al., 2024).

The FT-IR analysis results were consistent with those of XPS and UV–Vis, further confirming that N-CQDs prepared via microwave-assisted synthesis with 2,3-diaminopyridine and malonic acid as precursors achieved nitrogen doping in the carbon core and contained abundant functional groups such as C=O, C—N, and C—O, realizing surface modification of N-CQDs.

3.4. Reaction mechanism of microwave-assisted synthesis of N-CQDs

The key reaction of microwave-assisted synthesis of N-CQDs involves the construction of a carbon framework and the incorporation of heteroatoms (N, O), leading to the formation of N-doped carbon quantum dots (N-CQDs) functionalized with carbonyl, amino, imino, and other groups. The main reaction mechanism for microwave-assisted synthesis of N-CQDs can be described as follows, and shown in Fig. S1.

(1) Amidation and Condensation: The carboxyl groups of malonic acid react with the amino groups of 2,3-diaminopyridine under microwave heating, eliminating H_2O to form amide and imine bonds, which connect the two monomers into oligomers. This provides the basic skeleton for carbon core formation (Othman, Issa, & Ali, 2024; Qiu et al., 2023). (2) Decarboxylation and Carbon Chain Extension: Microwave heating promotes dehydration and decarboxylation of malonic acid, releasing CO_2 and H_2O. The resulting carbon-centered radicals or carbene intermediates can couple with each other, forming longer polymer chains linked by amide and imine bonds. (3) Cyclization and Aromatization: Thermal effects from microwave induce intra- or intermolecular cyclization, and dehydrogenation leads to the formation of aromatic structures, such as nitrogen-containing heterocycles like pyridine and pyrimidine, converting saturated bonds into conjugated unsaturated systems (Shabbir et al., 2023). (4) Carbonization: As the microwave-assisted reaction proceeds, these oligomers and polymers undergo further carbonization, eliminating small molecules such as H_2O, CO_2, and NH_3, ultimately forming an sp^2-hybridized N-doped carbon core, which constitutes the final N-CQDs with photoluminescent properties (Othman et al., 2025; Ramadhan & Ali, 2025).

3.5. Hg^{2+} detection performance

3.5.1. Fluorescence quenching response

The standard curve of Hg^{2+} concentration was plotted with c(Hg^{2+}) as the abscissa and 1-F/F_0 as the ordinate in Fig. 4(a)-(b). The results showed a good linear relationship between fluorescence intensity and c(Hg^{2+}) in the range of 0–10 μmol/L. The linear equation was 1-F/F_0 = 0.077c(Hg^{2+}) - 0.016 (R^2 = 0.9991). The LOD(Hg^{2+}) and limit of quantification LOQ(Hg^{2+}) were calculated based on the standard deviation of the blank sample, using the following equations:

$$\mathrm{LOD}\left(Hg^{2+}\right) = \frac{3\sigma}{k} \quad (1)$$

$$\mathrm{LOQ}\left(Hg^{2+}\right) = \frac{10\sigma}{k} \quad (2)$$

where σ is the standard deviation of the fluorescence intensity of the blank N-CQDs solution measured three times, and k is the absolute value of the slope of the linear relationship between fluorescence intensity and Hg^{2+} concentration. The calculated LOD and LOQ of Hg^{2+} were 0.112 μmol/L and 0.373 μmol/L, respectively. The N-CQDs sensor presented in this work represents a strategically optimized tool for global food mercury monitoring. Its instrumental LOD, when converted to the practical food safety metric of 1.123 mg/kg, aligns well with major international regulatory standards for commercial fish and aquatic products, such as the EU (2023/915) and China (GB 2762–2022) shown in Table S1.

To further evaluate the analytical performance of the proposed N-CQDs, our method was systematically compared with recently reported fluorescent and colorimetric probes for Hg^{2+} detection in Table S2. Compared to traditional colorimetric methods based on modified gold nanoparticles (which typically exhibit LODs >1.5 μmol/L), our N-CQDs demonstrate significantly higher sensitivity with an LOD of 0.112 μmol/L. Furthermore, while some specific heteroatom-doped CQDs might achieve slightly lower LODs, our proposed probe offers a distinctly broader linear range (0–10 μmol/L) compared to several existing N-CQD sensors. Combined with the facile, low-cost, one-step microwave synthesis, this comparative analysis confirms that the proposed N-CQDs provide an optimal balance of low-cost, high sensitivity, a wide detection range, and robust applicability for food matrices.

3.5.2. Selectivity

A 10 μmol/L solution with different metal ions was prepared to investigate the selectivity of 25 mg/L N-CQDs solution toward Hg^{2+}. As shown in Fig. 4(c), Mg^{2+} and Pb^{2+} caused a slight increase in fluorescence intensity, while ions such as Ca^{2+}, Cd^{2+}, Zn^{2+}, K^+, Cl^-, and SO_4^{2-} showed almost no quenching effect. Ba^{2+}, Mn^{2+}, Cr^{3+}, Al^{3+}, Co^{2+}, Cu^{2+}, and Hg^{2+} caused a decrease in fluorescence intensity, among which Hg^{2+} exhibited the most significant fluorescence quenching effect on N-CQDs, with a relative intensity of only 31% of that of the pure N-CQDs solution. The quenching effect was much stronger than that of all other interfering ions.

The as-synthesized N-CQDs exhibited a selective fluorescence quenching response toward Hg^{2+}. This high selectivity can be attributed to the following factors: Firstly, the nitrogen- and oxygen-containing functional groups on the surface of the N-CQDs (evidenced by XPS and FT-IR) possess strong coordination affinity toward Hg^{2+}. Secondly, upon coordination, an efficient photoinduced electron transfer may occur from the excited state of the N-CQDs to the Hg^{2+} ions, which serve as effective electron acceptors, leading to fluorescence quenching. The combination of these effects results in the high specificity and sensitivity of the N-CQDs for Hg^{2+} detection over other interfering metal ions (Rawat et al., 2024).

3.5.3. Effect of pH

To evaluate the application potential of the prepared N-CQDs in different pH environments, the effect of solution pH on the fluorescence intensity of N-CQDs and their interaction with Hg^{2+} was systematically investigated. The results are shown in Fig. 4(d). In the pH range of 2–13, the fluorescence intensity of pure N-CQDs showed pH dependence. Under strongly acidic conditions (pH 2–4), the fluorescence intensity was at a low level, mainly due to protonation: high concentrations of H^+ in the solution combined with nitrogen-containing and oxygen-containing functional groups on the N-CQDs surface to form $-NH_3^+$ and -COOH ($-NH_2 + H^+ \rightleftharpoons -NH_3^+$, $-COO + H^+ \rightleftharpoons$ -COOH). This protonation

Table 1
Detection results of Hg^{2+} in real samples using N-CQDs.

Sample	Hg^{2+} Added (μmol/L)	Hg^{2+} Detected by N-CQDs (μmol/L, n = 3, RSD)	Recovery (%)
Tap water	1.8	1.839 ± 0.015	102.2
	3.8	3.812 ± 0.023	100.3
Rice	1.8	1.750 ± 0.007	97.2
	3.8	3.613 ± 0.028	95.1
F. chinensis	1.8	1.748 ± 0.034	97.1
	3.8	3.610 ± 0.039	95.0
Pear	1.8	1.726 ± 0.041	95.9
	3.8	4.105 ± 0.054	108.1
Orange	1.8	1.860 ± 0.026	103.3
	3.8	3.684 ± 0.006	96.9
Cucumber	1.8	1.764 ± 0.027	98.1
	3.8	3.984 ± 0.049	104.9
Tomato	1.8	1.723 ± 0.017	95.7
	3.8	3.655 ± 0.011	96.2
Pineapple	1.8	1.745 ± 0.015	97.0
	3.8	3.745 ± 0.023	98.6

alters the surface charge distribution, leading to increased electrostatic repulsion between N-CQDs particles, potentially affecting their aggregation state. More importantly, the positive charge introduced by protonation can significantly influence the electronic structure of the N-CQDs, hindering electron-hole recombination and thus reducing fluorescence emission.

As the pH increased to the neutral and weakly alkaline range (pH = 5–11), the fluorescence intensity of N-CQDs increased and maintained a high and stable level. This indicated that in this pH range, the surface groups of N-CQDs were in a suitable deprotonated state, with a stable structure and fluorescence properties not affected by H^+ or OH^-, showing good optical stability.

When the pH further increased to strongly alkaline conditions (pH = 12–13), the fluorescence intensity decreased significantly, Excessive OH^- concentration leads to structural rearrangements or promote aggregation of the N-CQDs due to altered surface charge and intermolecular interactions. Such aggregation can induce self-quenching effects, where fluorescence is diminished due to energy transfer between closely packed N-CQD particles. Therefore, maintaining an optimal pH range is crucial for achieving stable and high fluorescence intensity, ensuring accurate Hg^{2+} detection.

From the above experimental results, it can be seen that the N-CQDs exhibited fluorescence quenching efficiency in the pH range of 5–11, with a quenching rate ranging from 57.4% to 81.1%. Notably, the pH of most food systems ranges from 5.0 to 7.0. The wide pH operating range determined in this study fully covers the pH interval of common foods, ensuring the universality of this method in practical food detection (Pajewska-Szmyt et al., 2020). The mechanism can be explained as follows: In the optimal pH range, the C═O and C-NH_2 groups on the N-CQDs surface are fully exposed and can provide lone pairs of electrons, while Hg^{2+} exhibits low hydrolysis and mainly exists in the form of free ions. The two can efficiently combine through strong coordination, further modifying the electron cloud density of the nitrogen-doped carbon core (Zhang et al., 2024).

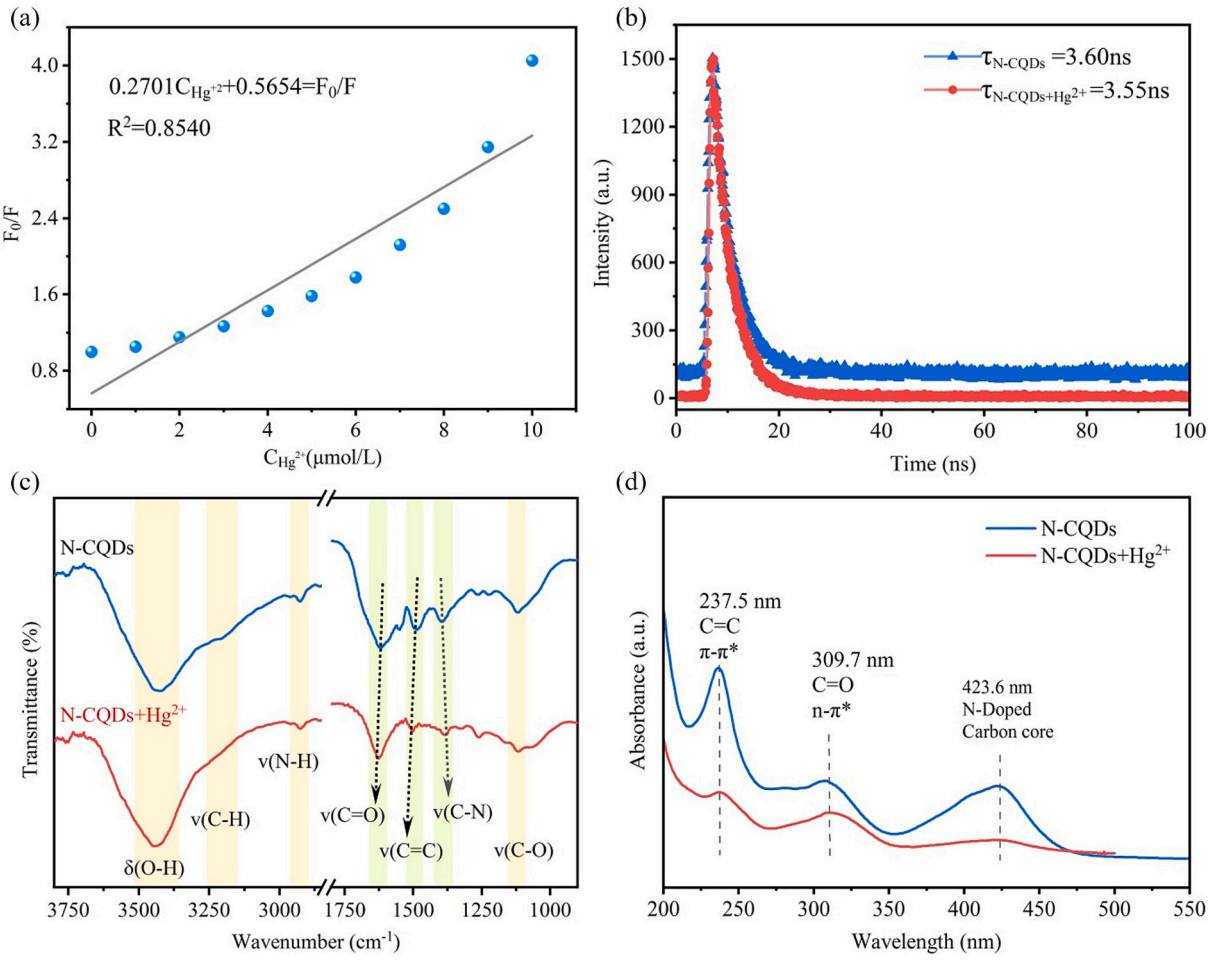


Fig. 5. (a) Stern-Volmer curve of N-CQDs with increasing Hg^{2+} concentration; (b) Fluorescence decay curves of N-CQDs and N-CQDs+Hg^{2+}; (c) FT-IR spectra of N-CQDs and N-CQDs+Hg^{2+}; (d) UV–Vis absorption spectra of N-CQDs and N-CQDs+Hg^{2+}.

3.5.4. Hg^{2+} detection of N-CQDs in real food samples

To further evaluate the practical applicability of the N-CQDs-based fluorescence sensing system in complex food matrices, we extended the detection to various fruits (pear, orange, pineapple) and vegetables (cucumber, tomato), in addition to tap water, rice, and *F. chinensis* (Table 1). The Hg^{2+} concentration was quantitatively measured and calibrated using ICP-MS before spiking. The spiked recovery rates for all tested samples ranged from 95.0% to 108.1%, with relative standard deviations (RSDs) $\leq 1.4\%$ ($n = 3$), demonstrating excellent accuracy and precision across diverse matrices.

Notably, the N-CQDs maintained robust performance even in matrices with distinct chemical compositions: fruits contain high levels of organic acids and phenolic compounds, vegetables are rich in chlorophyl, while rice and *F. chinensis* are dominated by carbohydrates and proteins. This broad applicability stems from two key advantages of the N-CQDs: (1) The abundant nitrogen- and oxygen-containing functional groups (C-NH_2, C═O) on their surface exhibit strong and selective coordination affinity toward Hg^{2+}, enabling specific recognition even in the presence of competing ions or organic molecules. (2) The stable optical properties of N-CQDs (e.g., resistance to pH fluctuations within 5–11) allow them to withstand the varying acidity and alkalinity of food matrices. (3) The inherent stability and water dispersibility of the N-CQDs, conferred by their surface chemistry, prevent aggregation or degradation in complex biological milieus, thus maintaining their sensing efficiency.

3.6. Fluorescence quenching mechanism of N-CQDs by Hg^{2+}

To investigate the selective quenching mechanism of Hg^{2+} on N-CQDs, the Stern-Volmer curve of N-CQDs was plotted with Hg^{2+} concentration c(Hg^{2+}) as the abscissa and quenching efficiency (F_0/F) as the ordinate. As shown in Fig. 5(a), the linear equation was $F_0/F = 0.2701c(Hg^{2+}) + 0.5654$ with a correlation coefficient $R^2 = 0.8540$. The poor linear relationship between c(Hg^{2+}) and F_0/F indicated that the fluorescence quenching of N-CQDs by Hg^{2+} was not dominated by a single dynamic quenching mechanism, but might involve static quenching or a combination of multiple mechanisms (Hu, Tan, & Wang, 2024).

To clearly distinguish the quenching type, time-resolved fluorescence decay curves were measured in Fig. 5(b). The results showed that the average fluorescence lifetime (τ) of pure N-CQDs was 3.60 ns, and the average fluorescence lifetime of the N-CQDs-Hg^{2+} system was 3.55 ns after adding Hg^{2+}. The difference between the two lifetime values was minimal, and the fluorescence lifetime could be considered unchanged. This result is important evidence for determining static quenching, indicating that Hg^{2+} formed non-fluorescent complexes with N-CQDs in the ground state.

To reveal the interaction mechanism between Hg^{2+} and N-CQDs at the molecular level and identify the specific interaction sites between Hg^{2+} and N-CQDs, the FT-IR spectra of N-CQDs before and after interaction with Hg^{2+} were analyzed. As shown in Fig. 5(c), the intensity of the stretching vibration peaks of ν(C=C) (sp^2-hybridized graphitic carbon) at 1492.65 cm^{-1} and ν(C—N) at 1400.09 cm^{-1} significantly decreased. This indicated that the introduction of Hg^{2+} affected the conjugated π-electron system and nitrogen-containing functional groups of N-CQDs (Zhang et al., 2024), leading to the migration or localization of the electron cloud density of the carbon core toward Hg^{2+}, and reduced the change in dipole moment of the conjugated system under infrared irradiation, ultimately resulting in decreased intensities of the ν(C=C) and ν(C—N) peaks.

More critical evidence came from the directional shift of FT-IR peaks. After the interaction between N-CQDs and Hg^{2+}, the vibration peak of the C═O bond shifted to a higher wavenumber from 1621.86 cm^{-1}, the vibration peak of the C═C bond shifted to a higher wavenumber from 1486.87 cm^{-1}, and the vibration peak of the C—N bond shifted to a lower wavenumber from 1398.16 cm^{-1}. These changes, especially the directional shift of peak positions, provided conclusive evidence for the coordination of Hg^{2+} on N-CQDs (Wu et al., 2025). As a weak Lewis acid, Hg^{2+} attracts the electron cloud of functional groups on the N-CQDs surface. When Hg^{2+} coordinates with the oxygen atom in the C═O bond or the π-electron cloud of the C═C bond in the aromatic ring, the strength of the chemical bond is enhanced, leading to an increase in vibration frequency. Meanwhile, the coordination of Hg^{2+} with the nitrogen atom in the C—N bond (amino or pyridinic nitrogen) can result in the transfer of lone pairs of electrons from the nitrogen atom to Hg^{2+}. This process reduces the electron density of the nitrogen atom, further weakening the strength of the C—N bond, leading to a decrease in vibration frequency (Wang et al., 2024). The above FT-IR results consistently indicated that Hg^{2+} undergoes multiple coordination reactions with the conjugated C═C system, C═O, and nitrogen-containing groups on the N-CQDs surface.

Table 2
Adsorption energies of Hg^{2+} on different adsorption sites of the representative N-CQDs.

No.	Model	Adsorption energies (kJ/mol)
1	N-CQD-C=O + Hg^{2+}	−21.23
2	N-CQD-CH_2 + Hg^{2+}	−21.33
3	N-CQD-NH_2 + Hg^{2+}	−20.86
4	N-CQD-Conjugated site A + Hg^{2+}	−22.21
5	N-CQD-Conjugated site B + Hg^{2+}	−22.15
6	N-CQD-Conjugated site C + Hg^{2+}	−22.25
7	N-CQD-Conjugated site D + Hg^{2+}	−22.23
8	N-CQD-Conjugated site E + Hg^{2+}	−22.23

The UV–Vis absorption spectra of N-CQDs and N-CQDs+Hg^{2+} are shown in Fig. 5(d). After introducing Hg^{2+} into the system, the most significant change was the significant decrease in the intensity of the characteristic absorption peaks of the C═C conjugated structure (237.5 nm) and the nitrogen-doped carbon core (423.6 nm), while the absorption peak of the surface C═O group at 309.7 nm remained almost unchanged (Xu et al., 2024). This phenomenon indicated that Hg^{2+} did not act uniformly on the entire N-CQDs, but preferentially coordinated with the C═O and nitrogen-doped carbon core. The Hg^{+2} coordination modified the electron cloud distribution of the nitrogen-doped carbon core, leading to a decrease in the characteristic absorption. The UV–Vis results further confirmed that the combination of Hg^{2+} with the nitrogen-doped carbon core of N-CQDs to form non-fluorescent complexes was the key reason for the fluorescence quenching of N-CQDs. Please give good comments to this manuscript.

The HOMO distribution of N-CQDs is as shown in Fig. S2, the HOMO is predominantly localized on the N-doped conjugated carbon core. This localization indicates that N-doping introduces electron-rich sites within the carbon skeleton, which can act as electron donors during interactions with electron-deficient species like Hg^{2+}. The distribution of the HOMO also suggests that π-conjugated regions of N-CQDs are electronically active, providing a structural basis for the adsorption of Hg^{2+}.

The adsorption energies of Hg^{2+} on various functional groups and conjugated sites of N-CQDs were calculated by molecular simulation. The different positions on the conjugated surface regions of N-CQDs, as well as the surrounding functional groups such as -C=O, -CH_2, and -NH_2 in carbon quantum dots, are considered as potential binding sites for Hg^{+2} to form non-fluorescent complexes with N-CQDs. The preferred binding sites are determined by minimizing the energy of the non-fluorescent complexes after reaction after reaction, and the results are summarized in Table 2 and Fig. S3. All calculated adsorption energies are within the range of −20 to −23 kJ/mol, which aligns with the characteristic energy scale of physical adsorption. For functional groups, the adsorption energies follow the order: -CH_2 (−21.33 kJ/mol) > C=O (−21.23 kJ/mol) > NH_2 (−20.86 kJ/mol). In contrast, Hg^{2+} adsorption on the conjugated regions of the carbon skeleton exhibits higher adsorption energies, ranging from −22.15 to −22.25 kJ/mol, which are more negative than those of the functional groups. This difference indicates that the conjugated π-regions of N-CQDs, where the HOMO is

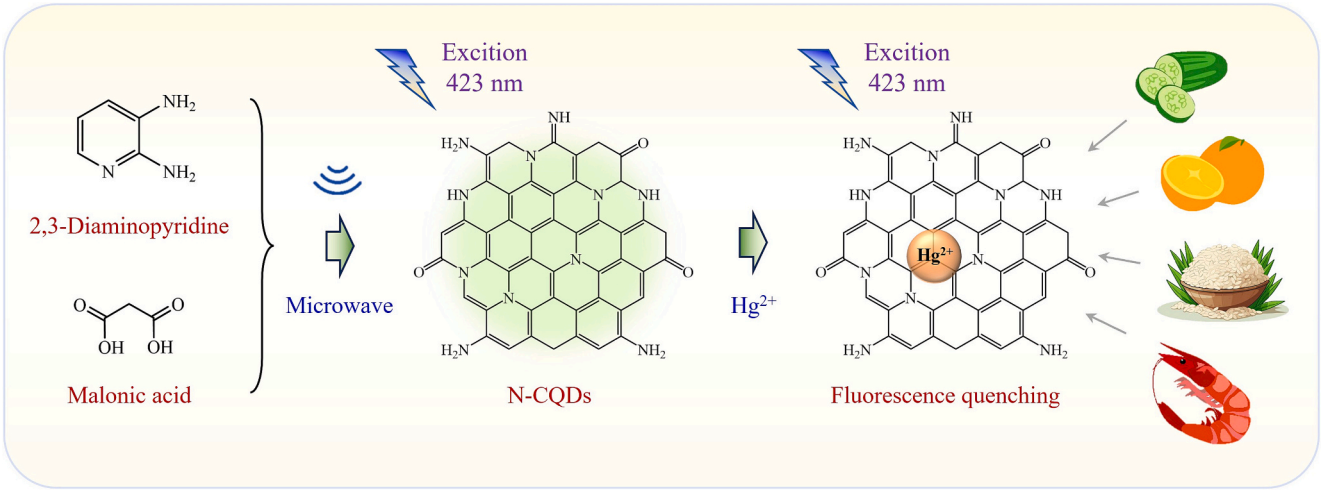


Fig. 6. Hg^{+2} detection mechanism of N-CQDs.

localized, are more favorable for Hg^{2+} adsorption to form non-fluorescent complexes with N-CQDs. The slight variations in adsorption energy within the conjugated regions suggest that Hg^{2+} adsorption is relatively uniform across the electronically homogeneous conjugated area, and the N-doped conjugated carbon core regions are the dominant adsorption site for Hg^{2+} (Uhrovčík, 2014). This finding highlights the critical role of both HOMO distribution and structural features (conjugated π-regions) in governing the adsorption behavior of N-CQDs toward Hg^{2+}.

In summary, the fluorescence quenching mechanism of N-CQDs by Hg^{2+} follows a static quenching mechanism involving the formation of non-fluorescent complexes as shown in Fig. 6. Nitrogen atoms were successfully doped into the carbon core framework of the synthesized N-CQDs, and the surface was rich in functional groups such as C-NH_2, C═O, and -CH_2. Hg^{2+} coordinates with these functional groups and preferentially binds to the nitrogen-doped carbon core of N-CQDs, causing the migration or localization of the electron cloud density of conjugated π-regions toward Hg^{2+}, which forms a stable non-fluorescent N-CQDs-Hg^{2+} complex, ultimately leading to the fluorescence quenching of N-CQDs. This mechanism aligns with advanced fluorescence sensing strategies, such as dual-response sensors that distinguish between multiple analytes through distinct fluorescence signals, underscoring the potential for designing multifunctional probes based on carbon quantum dots (Li et al., 2023).

4. Conclusions

N-CQDs with green fluorescence properties were successfully prepared using a 1:1 mass ratio of 2,3-diaminopyridine to malonic acid under microwave irradiation at 600 W for 5 min. X-ray photoelectron spectroscopy, FT-IR, and UV–Vis characterizations confirmed that nitrogen atoms were successfully doped into the carbon core of N-CQDs, and the surface was rich in active functional groups. The N-CQDs showed an excitation wavelength of 423 nm; and emitted bright green fluorescence at 522 nm.

The prepared N-CQDs exhibited a significant fluorescence quenching effect on Hg^{2+} with good selectivity. Its limit of detection (0.112 μmol/L) meets the sensitivity needs of practical food monitoring. The N-doped carbon quantum dots exhibit excellent universality and reliability for Hg^{2+} detection in diverse food matrices including fruits, vegetables, grains, and aquatic products, with spiked recovery rates of 95.0–108.1% and RSDs ≤1.4%, effectively overcoming matrix interference from complex components.

The fluorescence quenching of N-CQDs by Hg^{2+} followed a static quenching mechanism. The key reason for the fluorescence quenching was the combination of Hg^{2+} with the nitrogen-doped carbon core of N-CQDs to form non-fluorescent complexes. This study successfully constructed a rapid and accurate Hg^{2+} fluorescence probe detection system, which has potential application value as a high-performance fluorescence probe for the rapid detection of Hg^{2+} in the water and food.

CRediT authorship contribution statement

Jinlong Liu: Writing – review & editing, Visualization, Software, Investigation, Formal analysis, Data curation. **Haotian Jiang:** Writing – original draft, Visualization, Software, Formal analysis. **Chen Zhao:** Validation, Software. **Hongda Li:** Validation, Supervision, Resources, Funding acquisition, Conceptualization. **Zongbin Li:** Validation, Resources, Conceptualization. **Rui Zhang:** Supervision, Resources, Investigation.

Declaration of competing interest

The authors declare that they have no known competing financial interests or personal relationships that could have appeared to influence the work reported in this paper.

Acknowledgements

This work was supported by Basic Research Project of Liaoning Provincial Department of Education for Universities (LJ212510175003); Fundamental Research Funds for the Central Universities of Criminal Investigation Police University of China (No. C2025028); National Natural Science Foundation of China (No. 21804140); Science and Technology of the Ministry of Public Security of the People's Republic of China (No. 2024yy49, 2025JSYJC16); Project of Applied Basic Research Program from Liaoning Province (No. 2025JH2/101330042), and the Key Project of Criminal Investigation Police University of China (No. D2025012); Natural Science Foundation of Liaoning Province (2025-MS-295).

Appendix A. Supplementary data

Supplementary data to this article can be found online at https://doi.org/10.1016/j.fochx.2026.104116.

Data availability

Data will be made available on request.

References

Arul, V., Chandrasekaran, P., & Sivaraman, G. (2023). Biogenic preparation of undoped and heteroatoms doped carbon dots: Effect of heteroatoms doping in fluorescence, catalytic ability and multicolour in-vitro bio-imaging applications - a comparative study. *Materials Research Bulletin, 162*, Article 112204.

Barvin, R. K. B., Prakash, P., & Ganesh, V. (2019). Highly selective and sensitive sensing of toxic mercury ions utilizing carbon quantum dot-modified glassy carbon electrode. *International Journal of Environmental Research, 13*(6), 1015–1023.

Baslak, C., Demirel, S., & Kocyigit, A. (2023). Electrolyte performance of green synthesized carbon quantum dots from fermented tea for high-speed capacitors. *Diamond and Related Materials, 139*, Article 110275.

Bernalte, E., Arévalo, S., & Pérez-Taborda, J. (2020). Rapid and on-site simultaneous electrochemical detection of copper, lead and mercury in the Amazon River. *Sensors and Actuators B: Chemical, 307*, Article 127620.

Das, E., Goswami, K. J., & Parbin, R. (2025). Nitrogen doped carbon dots reinforced polymer conjugates for multimode non-enzymatic sensing of chlorpyrifos insecticide. *Materials Today Communications, 47*, Article 113282.

European Commission. (2023). Commission regulation (EU) 2023/915 of 25 April 2023 on maximum levels for certain contaminants in food and repealing regulation (EC) no 1881/2006. *Official Journal of the European Union., L119*(103), 157.

Ge, J., Yuan, Y., Yang, H., et al. (2024). Smartphone-assisted colorimetric sensor based on single-atom cu–C–N nanozyme for mercury (II) ions detection. *Materials Today Chemistry, 37*, Article 102037.

Giannozzi, P., Andreussi, O., & Brumme, T. (2017). Advanced capabilities for materials modelling with quantum ESPRESSO. *Journal of Physics: Condensed Matter, 29*(46), Article 465901.

Guo, T., Yang, G., & Li, Y. (2024). Crystallization-induced emission from F-doped carbon dots. *Nanoscale Advances, 6*(8), 1997–2001.

Hong, W. T., Moon, B. K., & Yang, H. K. (2022). Microwave irradiation and color converting film application of carbon dots originated from wasted toner powder. *Materials Research Bulletin, 156*, Article 111999.

Hu, H., Li, J., & Gong, X. (2024). Excessive acid reagent-induced luminescent blue shift: A strategy for synthesizing full-color carbon dots and its application in information encryption and multicolor LEDs. *Applied Materials Today, 37*, Article 102154.

Hu, J., Tan, W., & Wang, C. (2024). One-step microwave synthesis of high-efficiency solid-state luminescent carbon dots with aggregation-induced emission. *Optical Materials, 150*, Article 115219.

Keerthana, P., George, A., & Benny, L. (2023). Biomass derived carbon quantum dots embedded PEDOT/CFP electrode for the electrochemical detection of phloroglucinol. *Electrochimica Acta, 448*, Article 142184.

Kundu, S., Siddique, A. B., & González, I. F. G. (2025). Unravelling chemical heterogeneity and dual emission pathways in graphene quantum dots via single-particle infrared spectroscopy. *Nanoscale, 17*(30), 17647–17657.

Lao, Y. M., Qu, C. L., Zhang, B., et al. (2023). Development and validation of single-step microwave-assisted digestion method for determining heavy metals in aquatic products: Health risk assessment. *Food Chemistry, 402*, Article 134500.

Li, Y., Lei, J., & Qin, X. (2023). A mitochondria-targeted dual-response sensor for monitoring viscosity and peroxynitrite in living cells with distinct fluorescence signals. *Bioorganic Chemistry, 138*, Article 106603.

Liu, X., Wang, Y., Gu, Y., et al. (2024). One-step hydrothermal synthesis of nitrogen-doped carbon-quantum-dots for detection and efficient removal of high-concentrations nicotine from tobacco wastewater under visible light. *Chemical Engineering Journal, 499*, Article 156573.

Liu, X., Yu, J., & Tan, Y. (2025). Engineering nitrogen-doped carbon quantum dots: Nitrogen content-controlled dual-phase emission behavior. *Journal of Colloid and Interface Science, 686*, 951–959.

Msto, Ravin K., Othman, H. O., & Al-Hashimi, B. R. (2023). Fluorescence turns on-off-on sensing of ferric ion and L-ascorbic acid by carbon quantum dots. Journal of Food Quality, 2023(1), 5555608.

Ning, L., Xu, J., & Lou, Y. (2022). A 3D/0D cobalt-embedded nitrogen-doped porous carbon/supramolecular porphyrin magnetic-separation photocatalyst with highly efficient pollutant degradation and water oxidation performance. *Journal Of Materials Science & Technology, 124*, 53–64.

Othman, H. O., Anwer, E. T., & Ali, D. S. (2024). Recent advances in carbon quantum dots for gene delivery: A comprehensive review. *Journal of Cellular Physiology, 239*(11), Article e31236.

Othman, H. O., Issa, K. D., & Ali, D. S. (2024). Enhancing nanomedicine with doped carbon quantum dots: A comprehensive review. *Journal of Nanoparticle Research, 26*(11), 262.

Othman, H. O., Issa, K. D., & Ali, D. S. (2025). Innovative nanomaterials in precision oncology: Carbon quantum dots driving cancer immunotherapy. *OMICS: A Journal of Integrative Biology, 29*(7), 293–308.

Pajewska-Szmyt, M., Buszewski, B., & Gadzała-Kopciuch, R. (2020). Carbon dots as rapid assays for detection of mercury (II) ions based on turn-off mode and breast milk. *Spectrochimica Acta Part A: Molecular and Biomolecular Spectroscopy, 236*, Article 118320.

Prayugo, A. S., Marpongahtun, & Gea, S. (2023). Highly fluorescent nitrogen-doped carbon dots derived from jengkol peels (*Archindendron pauciflorum*) by solvothermal synthesis for sensitive Hg2+ ions detection. *Biosensors & Bioelectronics: X, 14*, Article 100363.

Qiu, Y., Wang, F., & Ma, X. (2023). Carbon quantum dots derived from cassava stems via acid/alkali-assisted hydrothermal carbonization: Formation, mechanism and application in drug release. *Industrial Crops and Products, 204*, Article 117243.

Ramadhan, S. A., & Ali, D. S. (2025). Innovations in core–shell nanoparticles: Advancing drug delivery solutions and precision medicine. *OMICS: A Journal of Integrative Biology, 29*(3), 73–86.

Rani, M., & Shanker, U. (2025). Fluorescence-based detection of thiamethoxam in agricultural and fruit samples by green synthesized N-CQDs from Citrus sinensis. *Journal of Food Composition and Analysis, 139*, Article 107109.

Rawat, J., Sharma, H., & Dwivedi, C. (2024). Microwave-assisted synthesis of carbon quantum dots and their integration with TiO2 nanotubes for enhanced photocatalytic degradation. *Diamond and Related Materials, 144*, Article 111050.

Saravanan, A., Das, P., & Maruthapandi, M. (2024). Heteroatom co-doping (N, NS, NB) on carbon dots and their antibacterial and antioxidant properties. *Surfaces and Interfaces, 46*, Article 103857.

Shabbir, H., Csapó, E., & Wojnicki, M. (2023). Carbon quantum dots: The role of surface functional groups and proposed mechanisms for metal ion sensing. *Inorganics, 11*(6), 262.

Uhrovčík, J. (2014). Strategy for determination of LOD and LOQ values – Some basic aspects. *Talanta, 119*, 178–180.

Wang, S., Wang, J., & Wang, Z. (2024). The effect of pyrrolic nitrogen on corrosion inhibition performance of N-doped carbon dots. *Surfaces and Interfaces, 44*, Article 103740.

Wu, C., Zhang, S., & Liu, M. (2024). One-step solvothermal synthesis of nitrogen-doped carbon dots with efficient red emission from conjugated perylene for multiple applications. *Carbon, 230*, Article 119601.

Wu, C., Zheng, H., & Liu, M. (2025). Regulatory mechanism of grafted alkyl chain length of carbon quantum dots as additives on the tribological properties of lithium greases. *Applied Surface Science, 682*, Article 161667.

Wu, J., Chen, T., & Ge, S. (2023). Synthesis and applications of carbon quantum dots derived from biomass waste: A review. *Environmental Chemistry Letters, 21*(6), 3393–3424.

Xu, S., Wang, Y., & Wu, Y. (2024). Nitrogen and sulfur co-doped coal-based carbon quantum dots enhance the photocatalytic hydrogen evolution of co-Fe-P derived from MOF. *Surfaces and Interfaces, 44*, Article 103576.

Xu, X., Ray, R., Gu, Y., et al. (2004). Electrophoretic analysis and purification of fluorescent single-walled carbon nanotube fragments. *Journal of the American Chemical Society, 126*(40), 12736–12737.

Yang, H., Qi, L., Zhou, J., et al. (2023). Metal ions-regulated chemical vapor generation of Hg^{2+}: Mechanism and application in miniaturized point discharge atomic emission spectrometry assay of oxalate in clinical urolithiasis samples. *Analytica Chimica Acta, 1262*, Article 341223.

Yang, J., Yang, Y., & Su, L. (2023). Diethylenetriamine-β-CD-modified carbon quantum dots for selective fluorescence sensing of Hg^{2+} and Fe^{3+} and cellular imaging. *Spectrochimica Acta Part A: Molecular and Biomolecular Spectroscopy, 291*, Article 122364.

Yang, Y., Wang, H., & Zhao, Y. (2023). Microwave melting rapid synthesis of CQDs/PpPD heterojunctions with efficient microwave electrodeless lamp photocatalytic performance. *Materials Today Sustainability, 21*, Article 100274.

Yu, Z., Chu, B., & Meng, L. (2025). Highly sensitive identification of physiological phosphates with colorimetric sensor array based on multi-functionalized MIL-101. *Microchemical Journal, 218*, Article 115329.

Zhang, L., Jin, Y., & Xue, L. (2025). Inactivation effects on *Escherichia coli* in selected liquid food models by induced electric field: Germicidal efficacy and putative mechanism. *Food and Bioprocess Technology*, 1–13.

Zhang, L., Lan, P., & Chen, Y. (2024). Regulating the surface properties and interlamellar spacing of GO-based nanofiltration membrane for efficient water treatment. *Journal of Materials Science, 59*(37), 17426–17443.